

See discussions, stats, and author profiles for this publication at: <https://www.researchgate.net/publication/231701581>

Microphase Separation and Phase Diagram of Concentrated Diblock Copolyelectrolyte Solutions Studied by Self-Consistent Field Theory Calculations in Two-Dimensional Space

ARTICLE *in* MACROMOLECULES · SEPTEMBER 2011

Impact Factor: 5.8 · DOI: 10.1021/ma2010266

CITATIONS

5

READS

39

4 AUTHORS, INCLUDING:



Yi-Xin Liu

Fudan University

11 PUBLICATIONS 180 CITATIONS

SEE PROFILE

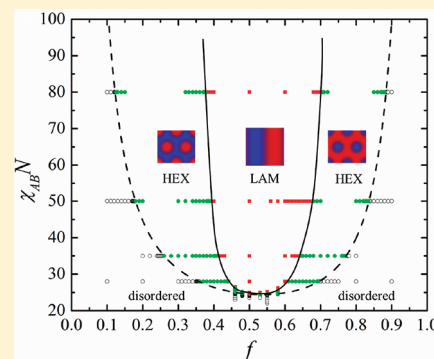
Microphase Separation and Phase Diagram of Concentrated Diblock Copoelectrolyte Solutions Studied by Self-Consistent Field Theory Calculations in Two-Dimensional Space

Yi-Xin Liu,^{*,†} Hong-Dong Zhang,^{*,†} Chao-Hui Tong,[‡] and Yu-Liang Yang[†]

[†]Key Laboratory of Molecular Engineering of Polymers of Ministry of Education, Department of Macromolecular Science, Fudan University, Shanghai 200433, China

[‡]Department of Physics, Ningbo University, Ningbo 315211, China

ABSTRACT: The self-consistent field theory (SCFT) is applied to the microphase separation of concentrated solutions of weakly charged polyelectrolytes. The generalized Poisson–Boltzmann equation describing the electrostatic interactions at the mean-field level is numerically solved by a full multigrid algorithm, which enables one to solve the SCFT equations of polyelectrolyte systems in real space as efficient as neutral polymer systems. To demonstrate the power of the real-space numerical scheme, we consider a diblock copoelectrolyte consisting of a charged block and a neutral block in two-dimensional space. The phase diagram in the Flory–Huggins interaction parameter—the composition space is constructed by numerical calculations. The density distribution of polymer segments, the counterions, and the net charge of the ordered structures, namely the lamellar phase and the hexagonal phase, are intensively examined. The effects of the interaction parameter and the degree of ionization are examined carefully. The numerical scheme can be easily extended to 3D calculations, various chain architectures, various charge distribution models, and other statistics chain models such as the worm-like chain model without losing any computational efficiency.



INTRODUCTION

Polyelectrolytes, among the most important classes of polymers, have been widely used in industry and they are attracting increasing attentions in recent years due to their biorelated applications.^{1–3} When dissolved in polar solvents such as water, the ionization of chemical groups from polyelectrolyte chain backbones results in charged polymers and small counterions. The long-range Coulomb interactions between these charged species together with the short-range excluded volume interactions pose great challenges in theoretical study of polyelectrolyte systems. The challenges become more serious in particle-based methods such as the molecular simulation techniques, where computationally expensive algorithms are unavoidable as long as the long-range interactions are present.⁴ On the contrary, there is an efficient way to deal with the long-range Coulomb interactions in field-based theories, where the electrostatic interaction is converted to the short-range interaction by introducing the electrostatic potential into the partition function during the Hubbard–Stratonovich transformation.⁵

The self-consistent field theory (SCFT), the most accurate theory at the mean-field approximation level, is one of such field-based theories. It has become a standard technique for studying microphase separations of neutral block copolymers owing to the efforts of Matsen and Schick,⁶ Drolet and Fredrickson,⁷ and Rasmussen and Kalosakas⁸ on developing various highly efficient algorithms or delicate screening techniques either in real space or

in spectral space.^{5,9} However, SCFT has not been widely used to study microphase separations in polyelectrolyte systems. Very few examples are available in the literature. The first systematic construction of SCF formalism for polyelectrolytes is given by Borukhov et al. in the middle 1990s, where a set of SCFT equations and mean-field free energies were derived for polyelectrolytes with various charge distributions in good solvents using a path integral formulation.^{10,11} Random phase approximation (RPA) has been performed to calculate the monomer–monomer structure factor $S(q)$. Shi and Noolandi generalized the theoretical framework developed by Borukhov et al. to multi-component polyelectrolyte systems.¹² This approach was successfully applied to study the interface of a simple single-component polyelectrolyte solution. Wang and co-workers further extended the SCFT of polyelectrolytes to block copoelectrolytes and position-dependent dielectric constant.¹³ The lamellar phase of a symmetric diblock polyelectrolyte solution has been examined in detail by solving the SCFT equations numerically. Kumar and Muthukumar applied the SCFT calculations to investigate the dependence of the counterion distribution on the interaction parameter for the lamellar phase of a diblock copoelectrolyte.¹⁴ The transition boundaries of the disorder–lamellar

Received: May 5, 2011

Revised: September 7, 2011

Published: September 27, 2011

transition, the cylinder-lamellar transition, and the sphere-cylinder transition were calculated based on RPA analysis. Recently, Yang et al. extended the reciprocal-space SCFT method originally devised by Matsen and Schick⁶ to the polyelectrolyte systems, where phase diagrams of A–B diblock copolyelectrolytes and A–B–A triblock copolyelectrolytes, both with A blocks being charged, were calculated.¹⁵ To date, however, there is still lack of an efficient real-space SCFT method for studying the phase separation of charged polymers other than in one-dimensional (1D) space. This is mainly due to lack of a time-efficient algorithm to solve SCFT equations when the generalized Poisson–Boltzmann (PB) equation is involved. Nevertheless, real-space SCFT methods do not require any a priori knowledge of symmetry, which becomes a great advantage when one wants to search new phase structures. In addition, the morphology of the equilibrium phase is a natural consequence of the real-space calculation, which provides important information for both theoretical and experimental researchers. For instance, the distribution of solvent molecules and counterions can be directly obtained by analyzing the morphology.

In this article, by introducing the full multigrid algorithm (FMG) to solve the PB equation, we develop a real-space numerical scheme which can solve the SCFT equations of the charged polymer system as efficient as the neutral polymer system. The numerical scheme is highly extensible and it is feasible to solve the SCFT equations in both two-dimensional (2D) and three-dimensional (3D) spaces. In principle, polyelectrolytes with any architecture and with any number of blocks, each of which can be either charged or neutral, can be treated using this numerical scheme. In particular, a concentrated solution of a diblock copolyelectrolyte consisting of a negatively charged (A) block and a neutral (B) block has been considered in this work. A phase diagram was constructed based on 2D SCFT calculations for the chosen system. In addition to the lamellar phase (LAM), the hexagonally packed cylinder phase (HEX) has been analyzed in detail.

THEORETICAL METHODS

A. SCFT Formalism. Here, we sketch a general theoretical framework for a concentrated solution of diblock copolyelectrolytes containing n_C polymer chains and n_S solvent molecules with or without salts. Each A–B copolymer has N total statistical segments with the volume fractions f and $1 - f$ for A and B blocks, respectively. It is supposed that the polymer segment and the solvent molecule have the same density ρ_0 , and the volume of small ions is ignored. We use subscripts A, B, S, +, and – in variables to denote A segments, B segments, solvent molecules, cations, and anions, respectively. The valences of charged species are represented by integer variables z_i ($i = A, B, +, \text{ and } -$).

To construct the statistical field theory for this charged system, we adopt the continuous Gaussian chain model. The smeared charge model is introduced to describe the charge distribution. In this model, charges are assumed to distribute uniformly along the chain contour. One example that should be well described by this model is the strongly dissociating polyelectrolyte, such as poly(acrylic acid) (PAA). In addition, the primitive model is used to describe the electrostatic interactions between two point charges mediated by the solvent. The solvent is considered as a continuous medium with a dielectric constant. With the above considerations, the free energy per chain of the system at volume

V and temperature T (in units of $k_B T$ where k_B is the Boltzmann constant) is given by¹³

$$F = \frac{1}{V} \int d\mathbf{r} [N \sum_K \sum_{L \neq K} \chi_{KL} \phi_K \phi_L - \sum_K w_K \phi_K - \eta (1 - \sum_K \phi_K)] - \frac{1}{V} \int d\mathbf{r} \frac{\epsilon}{2} |\nabla \psi(\mathbf{r})|^2 - \bar{\phi}_C \ln \frac{Q_C}{\bar{\phi}_C} - N \sum_M \bar{\phi}_M \ln \frac{Q_M}{\bar{\phi}_M} \quad (1)$$

Here, ϕ_K (ϕ_L) are density fields normalized by ρ_0 , and w_K are corresponding conjugate potential fields introduced to exert interactions on species K (L) ($K, L = A, B, \text{ and } S$); ψ is the electrostatic potential field; η is a Lagrange multiplier that ensures the incompressibility of the system; χ_{KL} denote the Flory–Huggins interaction parameters between species K and L ; ϵ represents the dielectric constant which is invariant across the whole system, and it is rescaled by $8\pi^2 \epsilon_0 \rho_0 e^2 b^2 / 3$ with ϵ_0 the dielectric constant of vacuum, e the unit charge, and b the length of a statistical segment (Kuhn length); $\bar{\phi}_C \equiv n_C N / \rho_0 V$ and $\bar{\phi}_M \equiv n_M / \rho_0 V$ are the volume-averaged densities for the block copolymer and for species M ($M = S, +, \text{ and } -$), respectively. Note that the spatial quantities in eq 1 are rescaled by the radius gyration of an unperturbed Gaussian chain $R_g = b(N/6)^{1/2}$, i.e. $\mathbf{r}/R_g \rightarrow \mathbf{r}$ and $V/R_g^d \rightarrow V$ with d the dimensionality of the system. In eq 1, Q_C is the normalized single-chain partition function for copolymer and Q_M are the normalized single-particle partition functions for species M .

Minimization of the free energy (eq 1) with respect to ϕ_K leads to the equations of equilibrium potential fields $w_K(\mathbf{r}) = N \sum_{L \neq K} \chi_{KL} \phi_L(\mathbf{r}) + \eta(\mathbf{r})$. Similarly, the equilibrium density fields can be obtained by minimizing the free energy with respect to w_j ($j = A, B, S, +, \text{ and } -$). They are given by $\phi_A(\mathbf{r}) = (\bar{\phi}_C / Q_C) \int_0^f ds q_C(\mathbf{r}, s) q_C^*(\mathbf{r}, 1 - s)$, $\phi_B(\mathbf{r}) = (\bar{\phi}_C / Q_C) \int_f^1 ds q_C(\mathbf{r}, s) q_C^*(\mathbf{r}, 1 - s)$, $\phi_S = (\bar{\phi}_S / Q_S) \exp[-w_S(\mathbf{r})/N]$, and $\phi_{\pm} = (\bar{\phi}_{\pm} / Q_{\pm}) \exp[-z_{\pm} \psi(\mathbf{r})]$. $q(\mathbf{r}, s)$ is a forward chain propagator which corresponds to the probability of finding the end segment of the polymer chain of length sN starting from the A block at location \mathbf{r} , which satisfies the modified diffusion equation

$$\frac{\partial q(\mathbf{r}, s)}{\partial s} = \begin{cases} \nabla^2 q(\mathbf{r}, s) - [w_A(\mathbf{r}) + z_A \alpha_A N \psi(\mathbf{r})] q(\mathbf{r}, s), & \text{if } s \leq fN \\ \nabla^2 q(\mathbf{r}, s) - [w_B(\mathbf{r}) + z_B \alpha_B N \psi(\mathbf{r})] q(\mathbf{r}, s), & \text{if } s \geq fN \end{cases} \quad (2)$$

with the initial condition $q(\mathbf{r}, 0) = 1$. α_A and α_B in eq 2 denote the degrees of ionization of A and B blocks, respectively. The degree of ionization is defined as the number of unit charges per statistical segment. The backward chain propagator $q^*(\mathbf{r}, s)$ initiated from the end of the B block satisfies a diffusion equation similar to eq 2.¹³ The normalized single-chain partition function is given by $Q_C = (1/V) \int d\mathbf{r} q(\mathbf{r}, 1)$, while the normalized single-particle partition functions are given by $Q_S = (1/V) \int d\mathbf{r} \exp[-w_S(\mathbf{r})/N]$ and $Q_{\pm} = (1/V) \int d\mathbf{r} \exp[-z_{\pm} \psi(\mathbf{r})]$.

To complete the set of SCFT equations, one needs to minimize the free energy with respect to ψ to find the electrostatic potential in equilibrium. It is straightforward to show that the equilibrium electrostatic potential satisfies the following general Poisson–Boltzmann equation:

$$\nabla^2 \psi(\mathbf{r}) = -\frac{N}{\epsilon} [\alpha_A z_A \phi_A(\mathbf{r}) + \alpha_B z_B \phi_B(\mathbf{r}) + z_+ \phi_+(\mathbf{r}) + z_- \phi_-(\mathbf{r})] \quad (3)$$

B. Numerical Method. The above mean-field equations can be numerically solved by a quasi-Newton method with fast convergence and remarkable accuracy.¹³ However, the quasi-Newton method involves an inversion of a Jacobian matrix, which is an algorithm with $O(M^3)$ computational complexity where M is the scale of the problem. The scale of a problem is defined as the total number of grids that the space has been discretized into. For a 3D problem in a cubic cell, M is equal to L^3 , where L is the number of discrete points in each side of the cell. Therefore, a huge amount of operations, L^6 for 2D problems and L^9 for 3D problems, are required, so that only one-dimensional problems are feasible in practice based on the quasi-Newton method. To overcome this difficulty, here we turn back to the continuous steepest descent method⁵ which has been proven to be a simple but effective strategy. The set of SCFT equations are solved in a similar way as that described by Drolet and Fredrickson⁷ except the PB equation (eq 3). First, fields w_A , w_B , w_S , and ψ are initiated by random numbers or by preset values. Then the modified diffusion equations for both forward and backward chain propagators are solved by utilizing a pseudospectral algorithm with nearly ideal computational complexity $O(N_s M \ln M)$.⁸ After that, the density fields ϕ_i are evaluated from the known potential fields. These densities are used to produce new fields w_A , w_B , and w_S . The auxiliary field η is updated according to $\eta^{\text{new}} = \eta^{\text{old}} + \lambda_\eta(1 - \phi_A - \phi_B - \phi_S)$ where λ_η is a relaxation parameter controlling the strength of the incompressibility. Given that we have found an efficient way to solve the PB equation, the new electrostatic potential field can be constructed by a linear mixing of the solution of the PB equation and the old field. Above procedures form a typical computational unit of the continuous steepest descent strategy. The computational unit is then executed repeatedly until some stop criteria are eventually met.

If the solution of the PB equation is not taken into account, the most time-consuming step during each iteration is the solution of diffusion equations which involves at least $O(N_s M \ln M)$ operations where $N_s = 1/\Delta s$ is number of points the chain contour has been discretized with Δs the contour step. The PB equation reduces to a Poisson equation if the densities in the right-hand side of eq 3 are replaced by those of the previous iteration. Poisson equation is perhaps the most well-known linear differential equation. A large number of algorithms are available to solve it numerically, the complexity of which ranges from $O(M)$ to $O(M^3)$. In this work, we introduce the full multigrid algorithm (FMG) which is the most efficient one with optimal $O(M)$ complexity.^{16–18} In principle, only $O(M)$ operations are needed to solve eq 3 with FMG, which is negligible compared to that of solution of diffusion equations as long as $N_s \ln M \gg 1$, which is fulfilled in most cases. Remarkably, charged polymer systems can now be numerically solved in a time comparable to that of neutral polymer systems. In other words, the FMG enables us to calculate the phase behavior of charged polymer systems in both two-dimensional (2D) and three-dimensional (3D) space.

One of drawbacks of the multigrid method is that there is no such standard multigrid solver available. It is still a nontrivial task to implement multigrid method for a given problem. Only after the property of the differential equation has been well exploited, the proper smoothing operator, restriction operator, and interpolation operator, the most important components for a multigrid program, can be chosen. In this work, we have successfully implemented the FMG for eq 3. Each component in the program has been carefully tuned to give ideal performance. Specifically, we choose a red-black Gauss–Seidel relaxation scheme as the

smoothing operator, bilinear interpolation as the interpolation operator, and full-weighting restriction as the restriction operator.¹⁷ The periodic boundary condition is imposed on all levels. The correctness and accuracy of the implementation are verified by solving analytical-solvable Poisson equations by comparing numerical solutions with analytical solutions. To verify the efficiency of the FMG program, we perform a speed test on our FMG program and the software package MUDPACK-5¹⁹ on the same platform. We find that our implementation is 10–15% faster than MUDPACK-5.

C. Case Study: Charged-Neutral Diblock Copolymers in a Salt-Free Solution. To demonstrate the power of the numerical method, we consider a salt-free solution of charged-neutral diblock copolymers. In particular, we set $N = 400$, $\bar{\phi}_C = 0.8$, $z_A = -1$, $z_+ = 1$, and $\chi_{AS} = \chi_{BS} = 0$ (the solvent is a good solvent for both A block and B block). Other parameters z_B , α_B , z_- , and $\bar{\phi}_-$ are all 0 for the B block is neutral and no salt is added to the solution. By invoking the constraints of incompressibility and electroneutrality, other volume-averaged densities given by $\bar{\phi}_S = 0.2$ and $\bar{\phi}_+ = 0.8\alpha_A f$. With the above setup, we mainly investigate the effects of following three parameters: f , χ_{AB} , and α_A .

Numerical SCFT calculations are carried out in a 2D cell with periodic boundary conditions. The cell with physical sizes $l_x \times l_y$ is discretized into $L \times L$ lattices where $L = 2^m$ with a typical m of 7. The lattice spacings along the x and y directions are determined by $\Delta x = l_x/L$ and $\Delta y = l_y/L$. The typical lattice spacing in our calculations is $0.03R_g$. Note that here we intentionally use a much smaller lattice spacing than $0.1 - 0.2R_g$ which is typical for neutral polymer systems. The lattice spacing is small because l_x and l_y should be small to ensure that the cell contains only one or two periods of phase structure and L needs to be large because of FMG. The smaller lattice spacing also improves the accuracy of the solution though it consumes more computational time. The value of N_s used to discretize the chain length is fixed at 200. As long as the right-hand side of eq 3 is smooth enough (none of N/ϵ , α_A , and χ_{AB} is too large), the continuous steepest descent scheme is stable if the relaxation parameters are carefully chosen. A working group of relaxation parameter are 0.05 for updating the potential fields w_A , w_B and w_S , 0.1 for updating the electrostatic potential field ψ , and 10 for updating the auxiliary field η . Sometimes smaller relaxation parameters are needed to stabilize the algorithm, e.g., when the system is near phase boundaries, or the interactions (either Flory-type or electrostatic) are strong. In practice, the difference of mean-field free energies between two consecutive iterations and the total residual error¹³ are both monitored. We choose the total residual error being smaller than 10^{-9} as a stopping criterion. Typically, the stop criterion is met after about 5,000 iterations. For calculations close to phase boundaries, 50 000 or more iterations are needed to reach the comparable precision. The typical time needed to complete one such calculation is estimated to be $5000 \times 0.35/60 \text{ s} \approx 30 \text{ min}$ on a single 2.5 GHz CPU core.

■ RESULTS AND DISCUSSION

A. Asymmetric Phase Diagram. As described previously, the highly efficient FMG enables us to treat charged polymer problems as neutral polymer problems at least in the sense of the numerical computation. It becomes a routine work to construct phase diagrams of charged polymer systems in the $\chi_{AB}N \sim f$ parameter space by SCFT calculations. The phase diagram of a concentrated charged-neutral diblock copolyelectrolyte solution is presented in

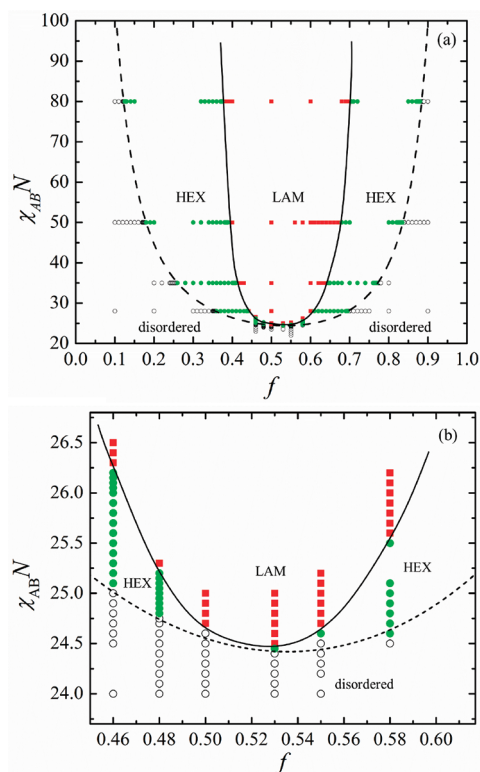


Figure 1. Phase diagrams of a concentrated salt-free solution of diblock copolyelectrolytes obtained by 2D SCFT calculations. The degree of ionization $\alpha_A N$ is fixed at 20. Key: red squares, LAM; green filled circle, HEX; black empty circle, disordered phase; dashed line, the spinodal line predicted by RPA theory; solid line, the HEX–LAM phase boundaries from 2D SCFT calculations.

Figure 1a, where we have successfully determined phase boundaries for three phases, namely the disordered phase, the cylindrical phase (HEX), and the lamellar phase (LAM), while those intrinsically 3D mesophases such as bcc spheres, close-packed spheres, and bicontinuous gyroid is unreachable in 2D calculations.

To locate phase boundaries in relatively high accuracies (0.001 for composition f and 0.1 for $\chi_{AB}N$), we have devised a two-stage scan scheme. At the first stage, the combinatorial screening technique⁷ with slight modifications is used to roughly determine the phase boundaries. The set of SCFT equations are solved in real space with random initial conditions. The calculations will converge to either stable or metastable phases. For high $\chi_{AB}N$ values, we fix $\chi_{AB}N$ and perform a scan from low f to high f with a step of 0.1 in a square cell. This scan path is parallel to the abscissa axis (f) and thus is called a parallel scan. Along the scan path, it is expected that we will encounter a disorder-to-cylinder transition (ODT), followed by a cylinder-to-lamellar transition (OOT), and then followed by two similar transitions in the reverse order. For lower $\chi_{AB}N$ values, $\chi_{AB}N$ instead of f is varied from low value to high value with a step of 0.5. This kind of scan is called a vertical scan since the scan path is parallel to the vertical axis ($\chi_{AB}N$). During the vertical scan, it will traverse an ODT followed by an OOT (sometimes the OOT will be bypassed as long as the gap between LAM and HEX is smaller than the scan step size). From these scans, we can roughly determine the phase boundaries.

At the second stage, the scans are narrowed to the region close to phase boundaries determined at the first stage. The SCFT

calculations are performed under given initial conditions. The fields $w_A(\mathbf{r})$ and $w_B(\mathbf{r})$ are initialized by random numbers if the disorder phase is expected, while they are initialized by a one-period 2D lamellar pattern if LAM is expected, and they are initialized by a two-period 2D hexagonal lattice pattern if HEX is expected. It should be noted that HEX is not compatible with the square cell due to the symmetry. Therefore, we will use a rectangle cell with $l_x:l_y = 2:(3)^{1/2}$ to perform calculations when HEX is expected. For all calculations, the field $w_S(\mathbf{r})$ is initialized by random numbers and the field $\psi(\mathbf{r})$ is initialized by 0. To determine the equilibrium phase for each point in the phase diagram, we also systematically vary cell sizes to eliminate the size effect of the simulation cell. The equilibrium phase at each point ($f, \chi_{AB}N$) is then assigned to the calculated phase structure with the lowest free energy. Each symbol in Figure 1a corresponds to such a determination of the equilibrium phase. The exact transition phase boundary should lie between two neighboring symbols of different phases, whose gap clearly determines the accuracy of the phase boundary.

To get a rough idea about how good our SCFT calculations are, we plot the spinodal line (the dashed line) of the concentrated solution predicted by random phase approximation (RPA) in Figure 1a. It can be seen that the binodal line (the phase boundary between the disorder phase and HEX) determined by our SCFT calculations and the spinodal line predicted by RPA theory are so close that they are indistinguishable. This behavior is typical for diblock copolymer melts,²⁰ and it also occurs in charged diblock copolymer melts.¹⁴ In the latter case, the binodal line and the spinodal line get closer and closer when either the degree of polymerization or the degree of ionization increases. Since our system is rather similar to the reported one and the similar behavior was actually observed, it implies that our SCFT calculations are indeed a valid tool for predicating of phase diagrams.

It is worth noting that the spinodal line in this article is obtained by conducting a stability limit analysis on the partial structure factor, $S_{AA}(q) = \langle \delta\phi_A(q)\delta\phi_A(-q) \rangle$ in Fourier space, which characterizes the spatial correlation of the concentration fluctuations of A blocks. The partial structure factor $S_{AA}(q)$ has the form²¹

$$NS_{AA}^{-1}(q) = NS_{\text{neutral}}^{-1}(q) + \frac{(\alpha_A N)^2}{\epsilon x + (\alpha_A N)f\bar{\phi}_C} \quad (4)$$

where $x = q^2 R_g^2$. The first term in the right-hand side of the above equation contains the contributions of all interactions except the electrostatic interaction, which is identical to the corresponding partial structure factor of the neutral diblock copolymer solution. This term can be derived from the linear response theory

$$S_{\text{neutral}}^{-1}(q) = \frac{1/\bar{\phi}_C + \vartheta N h_t + (\chi_{AB} N) h_{12} - (\chi_{AB} N)[(\chi_{AB} N) + 2\vartheta N]\bar{\phi}_C(h_1 h_2 - h_{12}^2/4)}{N[h_1 + \vartheta N\bar{\phi}_C(h_1 h_2 - h_{12}^2/4)]} \quad (5)$$

where h_1 is the Debye function defined as $h_1 = h(f, x) = 2(fx + e^{-fx} - 1)/x^2$, and $h_2 = h(1 - f, x)$, $h_t = h(1, x)$, and $h_{12} = h_t - h_1 - h_2$. In eq 5, $\vartheta = 1/\bar{\phi}_S - 2\chi_{PS}$ is an excluded volume parameter related to the short-range interactions between solvent molecules and polymeric segments. The second term in the right-hand side of eq 4 contains the contribution originated from the long-range Coulomb interactions at the Debye–Hückel level.

The partial structure factor $S_{AA}(q)$ possesses a maximum at a certain wavelength q_s whose value is independent of the segregation effects. However, the shape of $S_{AA}(q)$ strongly depends on the segregation effects. For neutral polymers, the controlling parameter is the product $\chi_{AB}N$ rather than the interaction parameter χ_{AB} alone, while for charged polymers, there is an additional parameter the product of the degree of ionization and the degree of polymerization $\alpha_A N$ due to the electrostatic interaction. Equations 4 and 5 clearly reveal these two kinds of dependencies. There is a critical value of $\chi_{AB}N$, $(\chi_{AB}N)_s$, beyond which the peak in $S_{AA}(q)$ diverges at $q = q_s$. $(\chi_{AB}N)_s$ is thus identified as the stability limit of the system. Unlike neutral polymers, the spinodal line in the $(\chi_{AB}N)_s \sim f$ plot is no longer universal but depends on the value of $\alpha_A N$. In other words, the spinodal line should remain unchanged as long as $\alpha_A N$ is fixed no matter how α_A and N are varied independently. Therefore, it can be considered as another type of universality specific to charged polymer systems. This assertion should be safely extended to all boundaries. We would like to emphasize that this kind of universality is an important feature of charged polymer systems that seems to be overlooked for years. Besides of $\chi_{AB}N$ and $\alpha_A N$, the dielectric constant ϵ is another interesting parameter that can influence the phase diagram of charged polymer systems as can be seen from the second term in the right-hand side of eq 4.

As the validity of the 2D SCFT calculation is established, it is ready for us to examine some properties of the phase diagram. The most obvious difference on the phase diagram between the charged polymer and the neutral polymer is that the ordered phase region of the former phase diagram is pushed upward. Taking $f = 0.5$ as an example, the interaction parameter of the critical point is 24.65 ± 0.05 as compared to 10.495 for neutral diblock copolymer melt and 13.119 for neutral diblock copolymer solution. The increase of the critical interaction parameter means that the miscibility of A and B blocks are enhanced by introduction of charges. Marko and Rabin suggested that the enhancement of miscibility is mainly due to the release of counterions of the charged polymer chains which significantly increases the mixing entropy.²² It should be pointed out that the electrostatic interaction among charged species have less important effect on the enhancement of miscibility than the release of counterions.

Another difference between the charged polymer system and the neutral polymer system is that the phase diagram of the charged polymer system is asymmetric. In Figure 1a, the asymmetry is not that obvious. RPA theory predicts that the degree of asymmetry will enhance with the increase of $\alpha_A N$.¹⁴ To illustrate the asymmetry clearly, the region near the critical point is amplified in Figure 1b. It can be seen that the composition f at the critical point shifts to 0.53 in this particular case (RPA theory predicts 0.536) as compared to 0.5 for neutral diblock copolymers. Moreover, the spinodal line, the binodal line, and the OOT boundary (solid lines in Figure 1) are all asymmetric. These asymmetries lead to the shift of HEX and LAM regions of the phase diagram toward high f end. In particular, the HEX region to the left of the critical point is enlarged and that to the right is contracted as seen in Figure 1a. This behavior is similar to the case in which the statistic segment length of the A block is larger than that of the B block.^{23,24} In contrast to the enhancement of miscibility, the asymmetry of the phase diagram is mainly caused by the electrostatic interaction.

These results may be very helpful for experimental studies. For diblock copolymers with one charged block, the critical point no longer locates at $f = 0.5$. Consequently, the equilibrium phase

near $f = 0.5$ is not necessary LAM. This fact may explain why HEX and gyroid were often observed near $f = 0.5$ in poly(styrene-sulfonate-*b*-methylbutylene) (PSS-PMB) copolymers where PSS is the charged block and PMB is the neutral block.^{25,26} The PSS blocks were prepared by randomly sulfonating PS blocks with a sulfonation level ranging from 10% to 50%. Since the sulfonic acid group is strongly acidic, PSS should be well described by the smeared charge model. Therefore, one can take the sulfonation level as the degree of ionization of PSS blocks. The degree of ionization in these samples is much higher than 5% used in our SCFT calculations, which should lead to much larger degree of asymmetry of the phase diagram than that shown in Figure 1a. Hence HEX will be the most possible equilibrium phase in the region between $f = 0.45$ and $f = 0.5$. In 3D space as in the experiments, gyroid phase is also possible. In light of the discussion on the universality of the controlling parameters ($\chi_{AB}N$ and $\alpha_A N$), it is important to note that the phase diagrams reported in ref 26 are very complicated since the product $\alpha_A N$ was not fixed in a same phase diagram. These phase diagrams can consist of phase boundaries with very strange shapes, depending on how N and α_A are varied.

On the basis of the above discussion, it can be concluded that our SCFT calculations qualitatively agree with the experimental findings. However, one should be aware that the Gaussian chain model may be no longer adequate for describing the chain statistics when the charge density on the chain becomes large (i.e., α_A is large). The large charge density on the chain will inevitably rigidify the chain, where the worm-like chain model should be more appropriate. Moreover, when the charge density on the polyelectrolyte chain exceeds some critical value, Manning condensation will occur and the charge density on the chain should be renormalized. To note further, our approach is in essential at the mean-field level, which means that the approach breaks down when multivalent ions are introduced because the correlation between those counterions can no longer be ignored. In this work, however, we are only interested in the cases where the Gaussian chain model still works. Meanwhile, only univalent counterions are considered. Incorporating the worm-like chain model into SCFT for charged polymer system should be the future work.

B. Structures of Ordered Phases. Although RPA theory can predict the equilibrium phase, it is unable to provide information about the underlying structures of the equilibrium phases, e.g., the density distributions of the A segments, the B segments, the solvent molecules, and the charged components (the free counterions and the charges distributed on the A blocks). On the contrary, the structure information is a direct consequence of the SCFT calculations. In literature, real-space 1D SCFT calculations are performed, where only 1D structure, i.e. lamellar phase, can be observed. In this work, real-space 2D SCFT calculations allow us to study an additional structure: HEX.

Figure 2 shows typical density distributions of the polymer segments and the solvent molecules, accompanied by the corresponding density distributions of the neutral diblock copolymer solution for the sake of comparison. It can be seen that the lamellar phase is resulted for the symmetrical charged diblock copolymer solution as expected. The system undergoes a micro-phase separation into two distinct domains: the neutral-block-rich domain (the left regions of Figure 2, parts a and c) and the charged-block-rich domain (the right regions of Figure 2, parts a and c). Similar to the neutral diblock copolymers, the density distributions in the A-rich domain and in the B-rich domain are perfectly symmetric. However, the interfaces between the A-rich

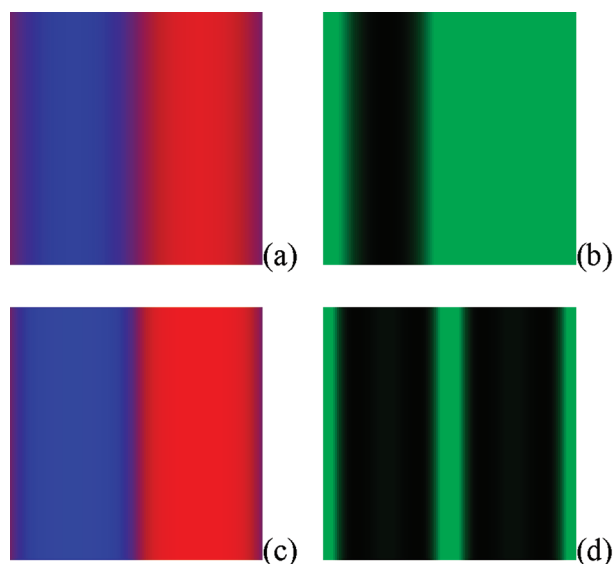


Figure 2. Density distributions of type A (red) and B (blue) segments (left columns), and solvent molecules (right columns) for charged-neutral diblock copolymer solutions (top row) and the same solutions of neutral diblock copolymers (bottom row) with $f = 0.5$, $\chi_{AB}N = 35$. The degree of ionization for charged blocks is $\alpha_A N = 20$. The cell sizes are (a, b) $2.7 \times 2.7 R_g^2$ and (c, d) $4.4 \times 4.4 R_g^2$. For all figures, the purer and the brighter the color is, the higher the corresponding concentration is. This applies to all following figures. The concentration of solvent has been rescaled according to $\hat{\phi}_S(\mathbf{r}) = [\phi_S(\mathbf{r}) - \min(\phi_S(\mathbf{r}))]/[\max(\phi_S(\mathbf{r})) - \min(\phi_S(\mathbf{r}))]$.

domain and the B-rich domain in the neutral diblock copolymer solution are much sharper than those in the charged diblock copolymer solution under the same condition, indicating that the miscibility of A and B blocks is enhanced by introducing charges. More interestingly, the solvent molecules not only prefer gathering in the interfacial region as they do in the neutral diblock copolymer solution but also prefer staying in the charged-block-rich domain. The solvent density is peaked at the center of the interface ($f = 0.5$) and decays more rapidly into the charged-block-rich domain than the neutral-block-rich domain, unlike the neutral diblock copolymer solution where the density decays symmetrically into both sides. Consequently, the solvent density is higher than the averaging value $\bar{\phi}_S$ in the interfacial region and in the charged-block-rich domain. For the charged polymer system, we also observed that the peak of the solvent density at the middle of the interface is pronounced. Meanwhile, the decay lengths are shortened. These observations suggest stronger segregation of the solvent molecules between the charged-block-rich domain and the neutral-block-rich domain. This kind of unbalanced distribution of solvent molecules in one lamellar period is first demonstrated here. The fluctuation of the solvent molecules may have some important consequences in practical situations such as the transportation of small ions.

Next, let us have a look at the charge density distribution of the free counterions and the net charge density distribution, which are shown in Figure 3a and 3b, respectively. The charge density distribution of the free counterions is equivalent to the density distribution of the free counterions since $z_+ = 1$. The net charge density is a local variable measured by $\phi_c(\mathbf{r}) = -\alpha_A \phi_A(\mathbf{r}) + \phi_+(\mathbf{r})$. It can be seen that the counterions can dissociate from polymer chains and diffuse into the neutral-block-rich domain. As a consequence,

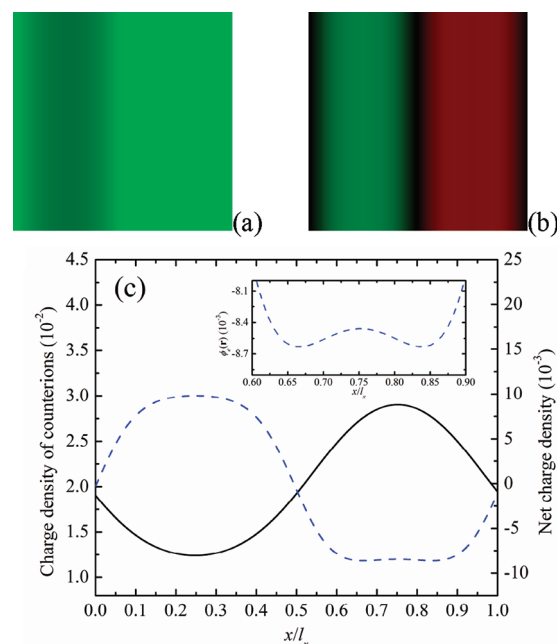


Figure 3. Charge density distribution of the free counterions (a) and the net charge density distribution (b) calculated by SCFT with the same parameters as those in Figure 2. The charge density of the free counterions is normalized by the averaging value $\bar{\phi}_+$ and rescaled by $\hat{\phi}_+(\mathbf{r}) = \phi_+(\mathbf{r})/\max(\phi_+(\mathbf{r}))$. The net charge density distribution is plotted in red for negative charges and in green for positive charges. It is normalized by $\hat{\phi}_c(\mathbf{r}) = |\phi_c(\mathbf{r})|/\bar{\phi}_+$. (c) Charge density profile of the free counterions (black solid line) and the net charge density profile (blue dash line) along the layer normal. The inset is a zooming in plot of the net charge density profile.

the overall charge in charged-block-rich domain is negative and it is positive in the neutral-block-rich domain. At the interfaces, the net charge density tends to be zero. In order to view the detailed variation of charge densities, we plotted the charge density profiles along the layer normal in Figure 2c. As shown in Figure 2c, the counterion charge density in the charged-block-rich domain is above the averaging value $\bar{\phi}_+ = 0.02$, while it is below this value in the neutral-block-rich domain. In contrast to the density distribution of the polymer segments, the charge density profiles are asymmetric. The charge density profile of the free counterions exhibits a broader peak in the neutral-block-rich domain than the peak in the charged-block-rich domain, whereas the net charge density profile behaves in an opposite manner. Although the electrical double-layers are not obvious in the net charge density profile, it will become more obvious when either $\chi_{AB}N$ or $\alpha_A N$ increases. In the net charge density profile, one can still identify a faint peak located at $x/l_x \approx 0.65$ rather than at $x/l_x = 0.5$ where the peak of the solvent density locates, implying that the electrical double-layer is actually formed. The decay of the peak (the one at $x/l_x \approx 0.65$) into the charged-block-rich domain is so slow that it interferes with the one decaying from the peak of the adjacent interface (the one at $x/l_x \approx 0.85$), leading to a broad peak at $x/l_x = 0.75$ (see the inset of Figure 3c). On the other hand, in the neutral-block-rich domain, the peak of the electrical double-layer in this domain is so broad that it overlaps the peak of the adjacent interface, leading to an overall broad peak. It is worth mentioning that we have also studied the dependencies of the charge densities on $\chi_{AB}N$ and $\alpha_A N$. The results are essentially the same as those

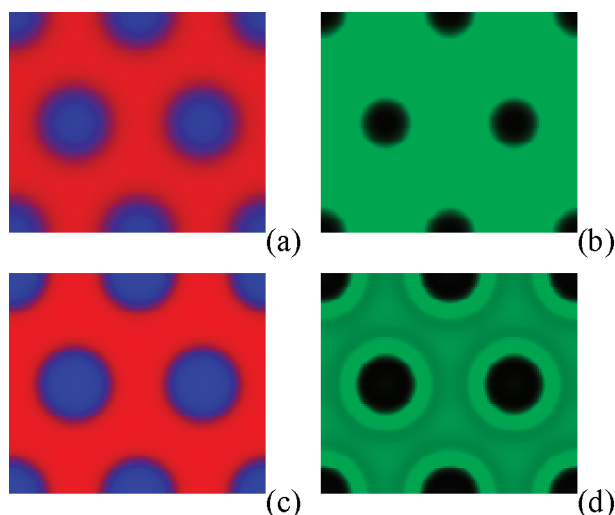


Figure 4. Density distributions of the A segments, the B segments (odd columns), and solvent molecules (even columns) for the charged-neutral diblock copolymer solution with $f = 0.7$ and $\alpha_A N = 20$. The interaction parameters $\chi_{AB}N$ are (a, b) 35 and (c, d) 50. The cell sizes are (a, b) $6.35 \times 5.50 R_g^2$ and (c, d) $7.27 \times 6.30 R_g^2$. The solvent density is scaled as described in Figure 2.

reported in ref 13 and 14 despite the fact that their results were obtained from 1D SCFT calculations.

When the composition f increases to 0.7, the charged-neutral diblock copolymer solution tends to phase separation into HEX phase with intermediate interaction parameters ($30 < \chi_{AB}N < 80$) according to the phase diagram in Figure 1a. Our 2D SCFT calculations enable the study of the detailed structure of the HEX phase. The typical morphologies for the HEX phase are presented in Figure 4. In order to be compatible with the symmetry of the HEX phase, the ratio of the width (l_x) and height (l_y) of the cell is fixed at 2: $(3)^{1/2}$. This kind of simulation cell can exactly contain two unit cells of the HEX phase. As expected, the density distributions strongly depend on $\chi_{AB}N$. The interfaces between the major phase (the charged-block-rich domain) and the minor phase (the neutral-block-rich domain) become sharper as $\chi_{AB}N$ increases (see Figure 4, parts a and c). Meanwhile, the maximum densities of the A and B segments approach the limited value $\bar{\phi}_C = 0.8$. The feature of the solvent density distribution is similar to the LAM phase; i.e., the solvent molecules are depleted from the neutral-block-rich domain and tend to gather in the interfacial region and in the charged-block-rich domain (see Figure 4, parts b and d). Moreover, the tendency of the segregation of solvent molecules between the major phase and the minor phase gets stronger and stronger as $\chi_{AB}N$ increases.

To uncover the details of the density distributions, we plot the density profiles along two specific directions (the x and y directions) for the morphologies presented in Figure 4, as shown in Figure 5. Instead of plotting the density profiles of the A and B segments individually, we plot the difference $\phi_A(\mathbf{r}) - \phi_B(\mathbf{r})$. Therefore, the positive part of the profile corresponds to the A-block-rich domain, i.e. the charged-block-rich domain. Intriguingly, one can observe that there is a weak minimum (at $y/l_y = 0$) of the density profile $\phi_A(\mathbf{r}) - \phi_B(\mathbf{r})$ in the charged-block-rich domain along the y direction (see Figure 5b), while for the LAM phase, no minimum exists within the charged-block-rich domain. This minimum is due to the symmetry of the HEX phase. For the solvent density

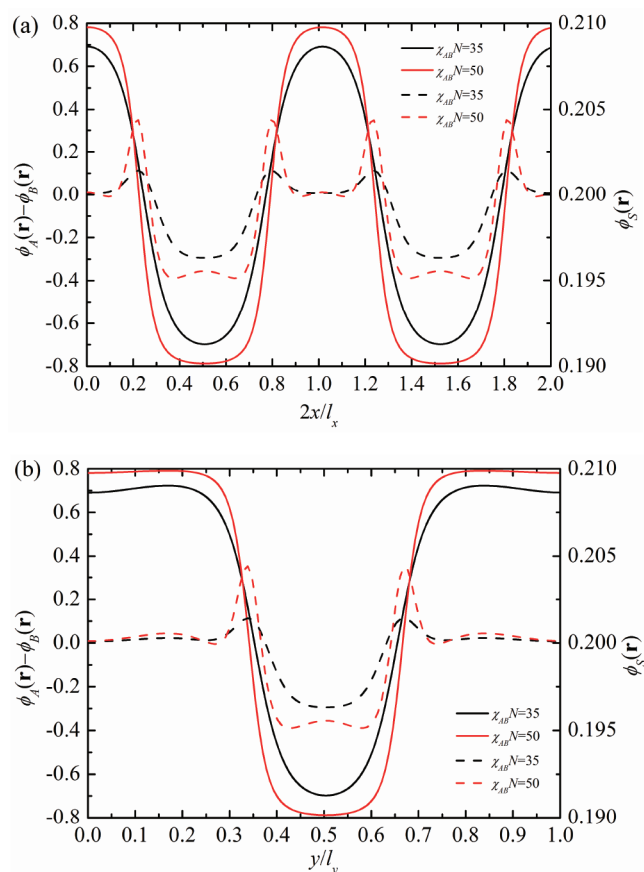


Figure 5. Density profiles of the A and B segments (solid lines) and the solvent (dash lines) along (a) the x direction and (b) the y direction across the center of the circular domain of the minor phase in Figure 4.

distribution, the deviation of the solvent density from the averaging value $\bar{\phi}_S$ in charged-block-rich domain is quite different from that in the neutral-block-rich domain. The density of the solvent is nearly identical to the averaging value in the charged-block-rich domain, while it is much below the averaging value in the neutral-block-rich domain. In other words, the excess solvent molecules in the interfacial region are mainly transported from the neutral-block-rich domain.

Like the LAM phase, we also analyzed the charge distributions of the HEX phase. The charge density distribution of the free counterions and the net charge density distribution are presented in Figure 6, and their density profiles along the x direction are given in Figure 7. Here, the effects of $\chi_{AB}N$ and $\alpha_A N$ on the charge density distributions are considered independently. Let us first look at the top row of Figure 6 where $\chi_{AB}N$ increases from 35 to 50 from the left column to the right column. On the one hand, at low $\chi_{AB}N$ close to the phase boundary, there are a considerable number of free counterions in the neutral-block-rich domains. As $\chi_{AB}N$ increases, more and more free counterions are restricted into the charged-block-rich domain, leading to sharper contrast of the charge density of the free counterions in the charged-block-rich domains and in the neutral-block-rich domains as shown in Figure 6, parts a and c. On the other hand, as $\chi_{AB}N$ increases, the density of the A segments saturates to the limited value $\bar{\phi}_C = 0.8$ to form a plateau in the density profile of the charged-block-rich domain. As a result, in the charged-block-rich domain, the gradual increase of the charge density of free counterions

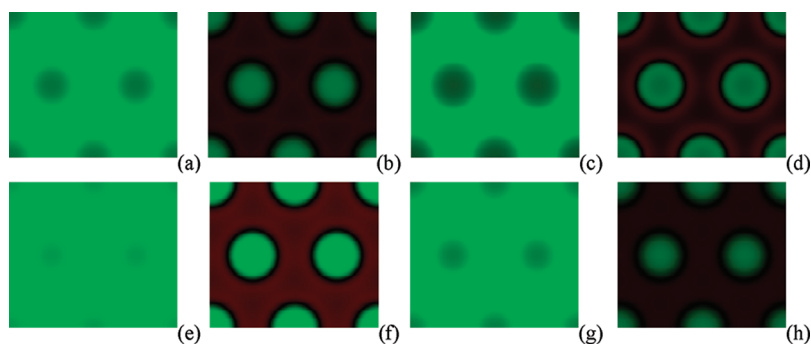


Figure 6. Charge density distribution of the free counterions (odd columns) and the net charge density (even columns) depend on the interaction parameter $\chi_{AB}N$ (top row) and the degree of ionization $\alpha_A N$ (bottom row) with $f = 0.7$. $\chi_{AB}N$ are (a, b, e–h) 35 and (c, d) 50. $\alpha_A N$ are (a–d) 20, (e, f) 4, and (g, h) 24. The cell sizes are (a, b) $6.35 \times 5.50 R_g^2$, (c, d) $7.27 \times 6.30 R_g^2$, (e, f) $8.66 \times 7.50 R_g^2$, (g, h) $5.89 \times 5.10 R_g^2$. The charge density of counterions and the net charge density are rescaled as described in Figure 3.

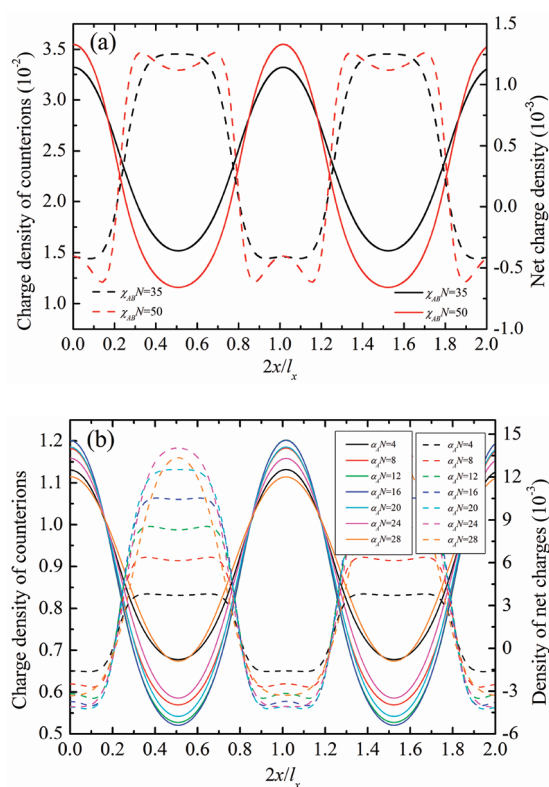


Figure 7. The dependences of the charge density profile of the free counterions (solid line) and the net charge density profile (dashed line) along the x direction on (a) the interaction parameter $\chi_{AB}N$ and (b) the degree of ionization $\alpha_A N$. $\alpha_A N = 20$ in part a; $\chi_{AB}N = 35$ in part b. The charge density of the free counterions is scaled according to $\bar{\phi}_+(\mathbf{r}) = \phi_+(\mathbf{r})/\bar{\phi}_+$ in part b. All other parameters are the same as those in Figure 6.

(bear positive charges) and the limited increase of the density of the A segments (bear negative charges) give a drop of the net charge density in the domain. The drop of the net charge density is clearly illustrated by the dark regions inside the green disks as shown in Figure 6d. The dark regions become darker and larger with increasing $\chi_{AB}N$. It has been proposed that all free counterions will be confined to the charged domains in the segregation limit ($\chi_{AB}N \rightarrow \infty$).¹⁴ Therefore, the dark regions will eventually occupy the whole area of the charged-block-rich

domains in the segregation limit, which results in electroneutrality everywhere.

Analysis of the charge density profiles gives the same extrapolation. Figure 7a shows the charge density profile of the free counterions and the net charge density profile along the x direction in Figure 6a–d, where one can easily identify the electrical double-layers at the interfaces. The peaks in the electrical double-layers become sharper as the miscibility of the A and B segments reduces. It is expected that in the segregation limit, these peaks become so sharp that their widths tend to 0, and the peaks with positive intensity cancels out the peaks with negative intensity. Consequently, the net charge density profile is stretched to a flat line parallel to the abscissa axis with $\phi_e(\mathbf{r}) = 0$.

As we already know, contrary to the interaction parameter $\chi_{AB}N$, the increase of the degree of ionization $\alpha_A N$ enhances the miscibility of the charged blocks and the neutral blocks. One may intuitively guess that $\alpha_A N$ will have an exactly opposite effect on the charge density distribution of the free counterions and the net charges density distribution as $\chi_{AB}N$ does. However, the case here is a little complicated since the degree of ionization directly controls the averaging value of the charge density of the free counterions via $\bar{\phi}_+ = 0.8f \alpha_A$. After the completion of the microphase separation, the charge density of the free counterions shall spatially fluctuate around the averaging value. To compare the charge density distribution of the free counterions at different degrees of ionization, we scale them by the averaging value $\bar{\phi}_+$ (see the caption of Figure 7b). Surprisingly, in the range of small degrees of ionization ($\alpha_A N \leq 0.04$), increasing $\alpha_A N$ leads to stronger segregation of counterions while the segregation of A and B blocks is weakened. Meanwhile, the electrical double-layers in the net charge density profiles are enhanced. The underlying mechanism of this unexpected phenomenon is not fully understood at present. We propose that the increase of $\alpha_A N$ must have two effects: one is to enhance the miscibility of the charge blocks and the neutral blocks; the other is to enhance the separation of counterions between the charged-block-rich-domain and the neutral-block-rich domain. For small degrees of ionization, the enhancement of the separation of counterions overwhelms the enhancement of miscibility, leading to the strong separation of the counterions. While for large degrees of ionization, the enhancement of the miscibility will take over the enhancement of the separation of counterions, so that the as-expected effect of $\alpha_A N$ should be restored (see the profiles with $20 < \alpha_A N < 28$ in Figure 7b). It is found that when $\alpha_A N > 28$, the equilibrium phase turns out to be homogeneous.

CONCLUSIONS

In this study, we developed a highly efficient numerical scheme for solving the SCFT equations containing a general Poisson–Boltzmann equation in real space. The introduction of the full multigrid algorithm drastically reduces the computational time for the solution of the PB equation. The time consumption is negligible in comparison with the solution of the modified diffusion equations. The power of this technique was demonstrated by performing a series of real-space 2D SCFT calculations to construct the phase diagram of a concentrated charged-neutral diblock copolymer solution.

The phase diagram of the charged-neutral diblock copolymer solution is asymmetric. The homogeneous phase is stabilized by introducing dissociable charges onto the polymer backbones. Increasing the degree of ionization ($\alpha_A N$) enlarges the parameter space of the homogeneous phase. Meanwhile, the critical point shifts to higher compositions (f). Consequently, the ODT phase boundary and the OOT phase boundaries are also lose their mirror symmetry. These changes of the phase diagram lead to larger parameter space for the HEX phase near $f = 0.5$, which can be used to explain the recent experimental results. Our numerical studies are consistent with the RPA theory, the 1D SCFT calculations, and the reciprocal-space SCFT calculations. The detailed structures of the ordered phases were examined. And the effects of the interaction parameter ($\chi_{AB} N$) and $\alpha_A N$ on the density distributions of the polymer segments, the solvent, and the charge components were analyzed systematically. It was found that the increase of $\chi_{AB} N$ and the decrease of $\alpha_A N$ have similar effects on the density distributions of the polymer segments and the solvent, while they influence the charge density distributions in a quite different manner.

Owing to the fact that the implementation of FMG is independent from the implementation of the continuous steepest descent scheme, the numerical approach developed in this work is highly extensible. For example, it is straightforward to apply it to explore ordered structures in 3D space, to study other chain architectures, other charge distribution models, and other statistics chain models such as the worm-like chain model (with this model, study of the strongly charged polyelectrolytes becomes possible). Furthermore, many other parameters, such as the dielectric constant, the concentration of the added salts, the concentration of the polymers, are all ready to be examined without altering the implementation. In addition, it is also valuable to analyze the domain spacings of the ordered structures, which can be directly obtained in real-space SCFT calculations. The dependences of the domain spacings on various controlling parameters will be reported elsewhere. We hope that the real-space SCFT technique devised in this work shall advance the SCFT study of the ordered structures in charged polymer systems on surfaces (2D), in membranes (2D), and in bulk (3D).

AUTHOR INFORMATION

Corresponding Author

*E-mail: liuyxpp@gmail.com (Y.X.L.); zhanghongdong@gmail.com (H.D.Z.).

ACKNOWLEDGMENT

The authors are grateful to Prof. An-Chang Shi and Dr. Jian-Feng Li for their discussions. This project is sponsored by Shanghai Postdoctoral Scientific Program (2011) and supported by the

National Nature Science Foundation of China (Grant Nos 20874019, 20990231, and 21074062).

REFERENCES

- (1) Hara, M., *Polyelectrolytes: Science and Technology*; Marcel Dekker, Inc.: New York, 1993.
- (2) Boudou, T.; Crouzier, T.; Ren, K.; Blin, G.; Picart, C. *Adv. Eng. Mater.* **2010**, *22*, 441.
- (3) Wong, G. C. L.; Pollack, L. *Annu. Rev. Phys. Chem.* **2010**, *61*, 171.
- (4) Dobrynin, A. V. *Curr. Opin. Colloid Interface Sci.* **2008**, *13*, 376.
- (5) Fredrickson, G. H. *The Equilibrium Theory of Inhomogeneous Polymers*; Oxford University Press: Oxford, U.K., 2006.
- (6) Matsen, M. W.; Schick, M. *Phys. Rev. Lett.* **1994**, *72*, 2660.
- (7) Drolet, F.; Fredrickson, G. H. *Phys. Rev. Lett.* **1999**, *83*, 4317.
- (8) Rasmussen, K.; Kalosakas, G. *J. Polym. Sci., Part B: Polym. Phys.* **2002**, *40*, 1777.
- (9) Matsen, M. W. Self-Consistent Field Theory and its Applications. In *Soft Matter*; Gompper, G.; Schick, M., Eds.; Wiley-VCH: Weinheim, 2006; Vol. 1.
- (10) Borukhov, I.; Andelman, D.; Orland, H. *EPL* **1995**, *32*, 499.
- (11) Borukhov, I.; Andelman, D.; Orland, H. *Eur. Phys. J. B* **1998**, *5*, 869.
- (12) Shi, A. C.; Noolandi, J. *Macromol. Theory Simul.* **1999**, *8*, 214.
- (13) Wang, Q.; Taniguchi, T.; Fredrickson, G. H. *J. Phys. Chem. B* **2004**, *108*, 6733.
- (14) Kumar, R.; Muthukumar, M. *J. Chem. Phys.* **2007**, *126*, 214902.
- (15) Yang, S.; Vishnyakov, A.; Neimark, A. V. *J. Chem. Phys.* **2011**, *134*, 54104.
- (16) Trottenberg, U.; Oosterlee, C. W.; Schüller, A. *Multigrid*; Academic Press: London, 2001.
- (17) Press, W. H.; Teukolsky, S. A.; Vetterling, W. T.; Flannery, B. P. *Numerical Recipes*; 3rd ed.; Cambridge University Press: Cambridge, U.K., 2007.
- (18) Yavneh, I. *Comput. Sci. Eng.* **2006**, *8*, 12.
- (19) Adams, J. C. *Appl. Math. Comput.* **1993**, *53*, 235.
- (20) Leibler, L. *Macromolecules* **1980**, *13*, 1602.
- (21) Benmouna, M.; Bouayed, Y. *Macromolecules* **1992**, *25*, 5318.
- (22) Marko, J. F.; Rabin, Y. *Macromolecules* **1992**, *25*, 1503.
- (23) Vavasour, J. D.; Whitmore, M. D. *Macromolecules* **1993**, *26*, 7070.
- (24) Matsen, M. W.; Bates, F. S. *J. Polym. Sci., Part B: Polym. Phys.* **1997**, *35*, 945.
- (25) Wang, X.; Yakovlev, S.; Beers, K. M.; Park, M. J.; Mullin, S. A.; Downing, K. H.; Balsara, N. P. *Macromolecules* **2010**, *43*, 5306.
- (26) Park, M. J.; Balsara, N. P. *Macromolecules* **2008**, *41*, 3678.